A Journal of the Gesellschaft Deutscher Chemiker

Angewandte International Edition GDCh Chemie

www.angewandte.org

Accepted Article

Title: H2S Donor Functionalized Molecular Machine for Combating Multidrug-Resistant Bacteria Infected Chronic Wounds

Authors: Yuan Chen, Kun-Mei Liu, Ling-Xiao Zhou, Jin-Yu An, Shun Feng, Ming-Yu Wu, and Xiao-Qi Yu

To be cited as: *Angew. Chem. Int. Ed.* **2025**, e202507833

Link to VoR: https://doi.org/10.1002/anie.202507833

WILEY VCH

10.1002/anie.202507833

WILEY VCH

RESEARCH ARTICLE

H_2S Donor Functionalized Molecular Machine for Combating Multidrug-Resistant Bacteria Infected Chronic Wounds

Yuan Chen[a,b], Kun-Mei Liu[b], Ling-Xiao Zhou[b], Jin-Yu An[b], Shun Feng*[b], Ming-Yu Wu*[a,b], Xiao-Qi Yu* [a,c]

[a] Y. Chen, Prof. M.-Y. Wu, Prof. X.-Q. Yu
School of Biomedical Engineering, Sichuan University, 610065 Chengdu, China
E-mail: wumy@scu.edu.cn; xqyu@scu.edu.cn

[b] Y. Chen, K. M. Liu, L. X. Zhou, J. Y. An, Prof. M.-Y. Wu, Prof. S. Feng
School of Life Science and Engineering, Southwest Jiaotong University, 610031 Chengdu, China
Email: fengshunxd@hotmail.com

[c] Prof. X.-Q. Yu
Asymmetric Synthesis and Chiral Technology Key Laboratory of Sichuan Province, Department of Chemistry, Xihua University, Chengdu 610039, P. R. China
E-mail: xqyu@scu.edu.cn

Supporting information for this article is given via a link at the end of the document.

Abstract: Chronic wounds are worldwide medical challenge due to the complex and multifaceted etiologies, including bacterial infection, persistent inflammation, and impaired angiogenesis. Developing a comprehensive strategy integrating antibiosis and anti-inflammation to promote revascularization and accelerate wound healing is highly desirable. Nevertheless, current therapeutic methods still face two major challenges: (1) how to combat bacterial drug resistance. (2) how to achieve spatiotemporal control over bacterial elimination and inflammation reduction. To address these issues, a novel H_2S donor functionalized molecular machine (MM), ACR-DM-HS, was developed. It selectively binds to and disturbs the bacterial membrane through a light-active vibronic-driven mechanochemical action (VDA), which synergizes with photodynamic therapy (PDT) to efficiently eradicate multidrug-resistant bacteria and biofilms, and conquers the evolution of bacterial resistance. Furthermore, it releases H_2S in infected tissues to scavenge excess reactive oxygen species (ROS), inhibit the secretion of inflammatory factors, promote angiogenesis and accelerate the healing of diabetic wounds *in vivo*. This work provides an integrated strategy combining antibiotic and anti-inflammation to treat with multidrug resistance bacterial infected chronic wounds.

Introduction

Chronic wounds, including diabetic ulcers, pressure ulcers, and venous ulcers, represent a worldwide medical challenge that significantly elevates amputation and mortality rates, imposing substantial health and social burdens.[1] The underlying complex and multifaceted etiologies, such as bacterial infection, persistent inflammation, and impaired angiogenesis are the primary contributing factors.[2] Clinically, combinations of antibiotics with surgical debridement and flap grafting are widely used therapeutic strategies. However, these approaches often suffer from the risks of persistent and recurrent infections and, more critically, unavoidable drug resistance.[3] To address these issues, advanced treatments such as chronic wound dressings, hydrogels, and multifunctional nano-enzyme materials have been developed to simultaneously deliver antibacterial and anti-inflammatory effects.[4]

To combat drug resistance, novel antibacterial strategies, such as antimicrobial peptides,[5] phage therapy,[6] PDT,[7] chemodynamic therapy,[8] photothermal therapy,[9] and immunotherapy,[10] have been incorporated into these composite materials. Nevertheless, these strategies still face challenges, including weak antibiofilm effects, exacerbation of inflammatory microenvironments due to excessive immune responses, and, most critically, the potential emergence of new resistance mechanisms through bacterial adaptive evolution, further complicating chronic wound management.[11]

In contrast to the aforementioned chemical or biological antibacterial methods, physical antibacterial approaches hold greater promise for circumventing bacterial resistance evolution.[12] Light-activated MMs represent a unique physical antibacterial strategy that employ light to induce whole-molecule vibrations and unidirectional rotation at the molecular scale, thereby generating VDA.[13] This mechanical action disrupts lipid bilayers, compromises membrane integrity, and impairs membrane function, resulting in irreversible bacterial death. Given that pathogenic microbes are unlikely to evolve defense mechanisms against such mechanical disruption, this approach has garnered increasing interest. However, to date, only Feringa-type unidirectional rotating molecular motors and cyanine-based MMs have been reported.[13,14] The field remains in its infancy, lacking efficient design strategies. Additionally, the mechanical effects of MMs often coincide with ROS generation, which may exacerbate inflammation in wound tissues and impede regeneration.[15]

To address the challenges of uncontrolled ROS production and excessive inflammation in chronic wounds, the integration of a potent antioxidant, anti-inflammatory, and pro-angiogenic agent is essential. Hydrogen sulfide (H_2S), a critical biological signaling

10.1002/anie.202507833

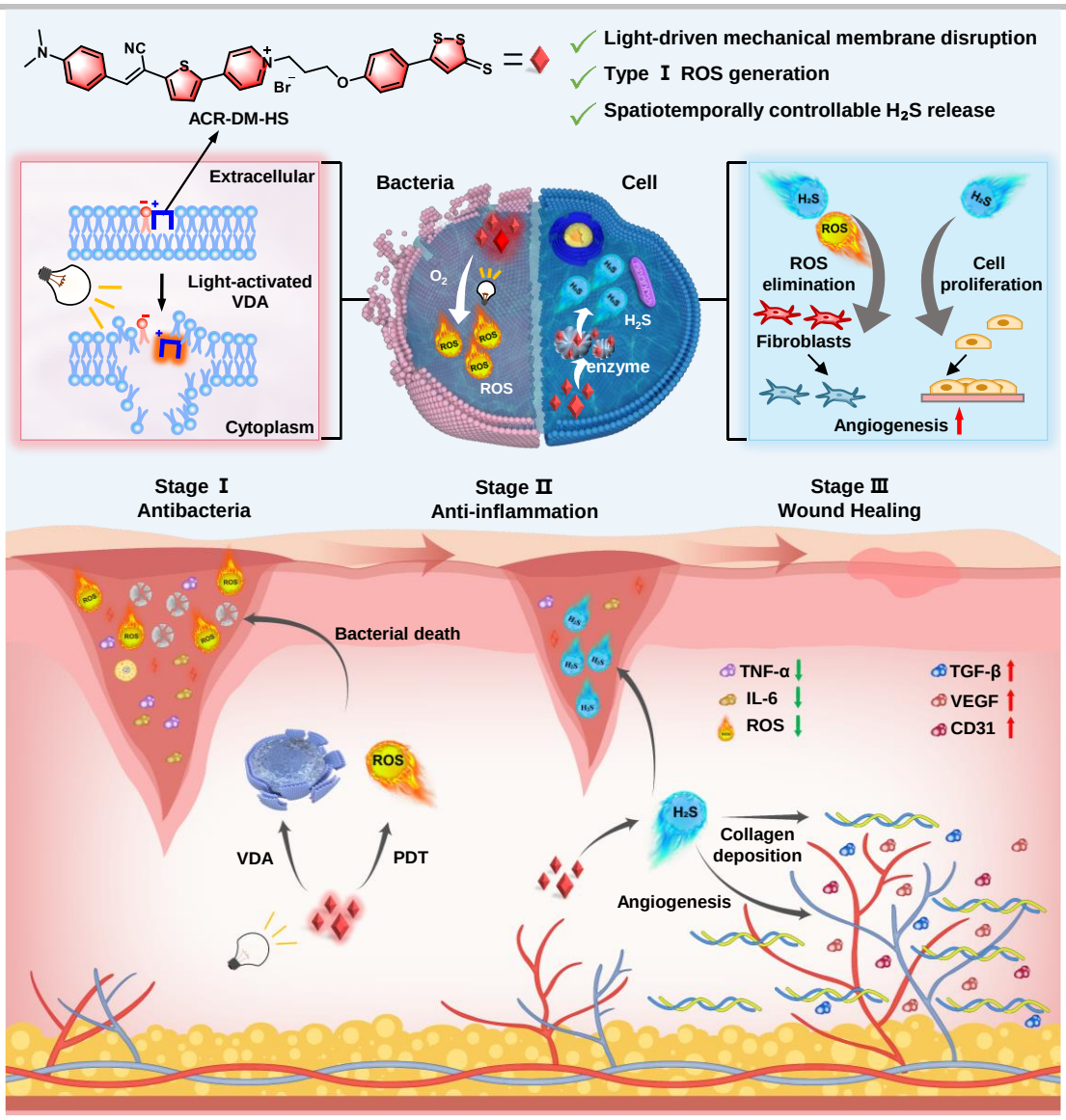

Scheme 1. Schematic illustration the chemical structure of light-activated MM, ACR-DM-HS, for chronic wound therapy via spatiotemporally controllable membrane disruption, ROS generation and H_2S releasing.

molecule, plays a pivotal role in modulating inflammation and stimulating angiogenesis.[16] It activates endogenous antioxidant defense mechanisms to mitigate oxidative stress, attenuates inflammation, and enhances cell proliferation and vascularization, thus accelerating wound healing.[17] Consequently, advanced materials combining PDT with H_2S donors have been developed for treating chronic wounds.[18] However, the H_2S release highly depend on the depletion of cysteine/glutathione, which may exacerbate oxidative stress in wound tissues. Furthermore, these combinatorial strategies lack spatiotemporal controllability, and H_2S may interact with ROS, compromising their individual and synergistic therapeutic effects and even potentially aggravating tissue damage.[19] Thus, designing a multifunctional MM capable of spatiotemporally controlled synergistic therapy for multidrug-resistant bacterial-infected chronic wounds represents a highly desirable yet challenging goal.

Herein, a lipophilic cationic MM functionalized with H_2S donor (ACR-DM-HS) was developed for spatiotemporally controllable synergistic therapy of chronic wounds. Compared with eukaryocytes, bacteria have a stronger negative membrane potential.[20] The lipophilic cationic ACR-DM-HS rapidly and selectively binds to bacterial membranes, disrupting their integrity and enhancing permeability via light-activated VDA, while concurrently killing bacteria through ROS produced by PDT. Subsequently, upon cellular uptake by infected or inflamed tissues, ACR-DM-HS releases H_2S via a mitochondria-enzyme-triggered mechanism, scavenging excess ROS, alleviating inflammation, and stimulating angiogenesis (Scheme 1). In an *in vivo* MRSA-infected diabetic ulcer model, ACR-DM-HS highly effectively eradicated MRSA and biofilms, reduced inflammatory cytokines, elevated proangiogenic factors, enhanced neovascularization, and activated fibroblasts to promote collagen deposition and accelerate wound healing. These results position

10.1002/anie.202507833

WILEY VCH

RESEARCH ARTICLE

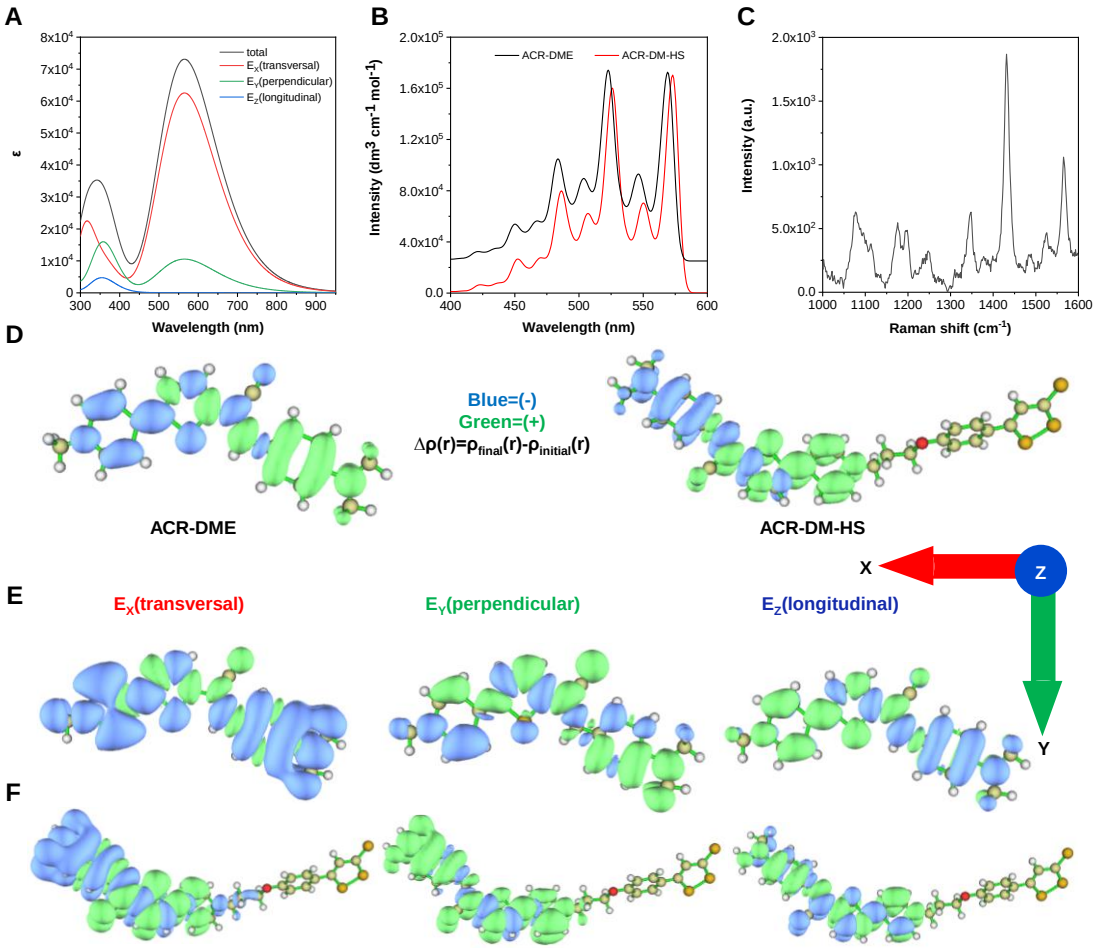

Figure 1. Vibrational excitation of MMs (ACR-DM-HS and ACR-DME). (A) The total and partial absorption spectra of ACR-DM-HS calculated by TD-DFT. (B) TD-DFT calculated vibrationally resolved absorption spectra of MMs in DMSO. (C) Raman spectrum of ACR-DM-HS. (D) TD-DFT calculated total induced charge densities [Δρ(r)] for molecular plasmon resonance. Δρ(r) by electric field (E_i) components oriented along the transversal, longitudinal and perpendicular axis of ACR-DME (E) and ACR-DM-HS (F). The vectors on the rightmost represent the orientation of the electric filed components.

ACR-DM-HS as a promising therapeutic candidate for multidrug-resistant bacterial-infected chronic wounds.

Results and Discussions

Molecules Design and Synthesis

Acrylonitrile served as the conjugated backbone. The incorporation of thiophene extended the π-conjugation system, promoting electron delocalization and enhancing global molecular vibrational properties. A robust donor-π-acceptor (D-π-A) architecture was engineered through synergistic integration of the electron-donating dimethylaniline moiety and the electron-withdrawing pyridinium group, which collectively amplified plasmonic enhancement effects and optimized vibration-driven molecular machine activity. The cationic pyridinium moiety facilitates electrostatic binding with anionic phospholipids on bacterial membranes, while the hydrophobic conjugated backbone and dimethylaniline interact with the lipid bilayer via hydrophobic insertion, synergistically enhancing bacterial binding affinity.[21] To mitigate the chronic inflammatory response in wounds and counteract the severe oxidative stress induced by excessive ROS, we introduced a mitochondrial enzyme-activated H_2S donor, ADT-OH, at the pyridinium termini, resulting in the successful development of ACR-DM-HS, a photoactivatable MM with integrated H_2S-generation capability. ACR-DM-HS was synthesized (Scheme S1) and characterized by ^{1}H NMR, ^{13}C NMR, and HRMS (Figures S1-S3). For comparison, ACR-DME, lacking the H_2S donor, was also synthesized following our previous protocol. [22]

Vibronic Driven Mechanochemical Action of MM

Upon light irradiation, valence electrons in the MM undergo photoexcitation from the ground state to the singlet excited state. Through electron-phonon coupling, the collective plasmonic oscillations experience rapid energy dissipation via non-radiative Landau damping (Figure S4). Subsequent vibronic relaxation during internal conversion induce coherent nuclear motions, thereby activating molecular vibrational eigenmodes. This VDA generates localized shear stresses taht disrupt lipid bilayer integrity.[13]

10.1002/anie.202507833

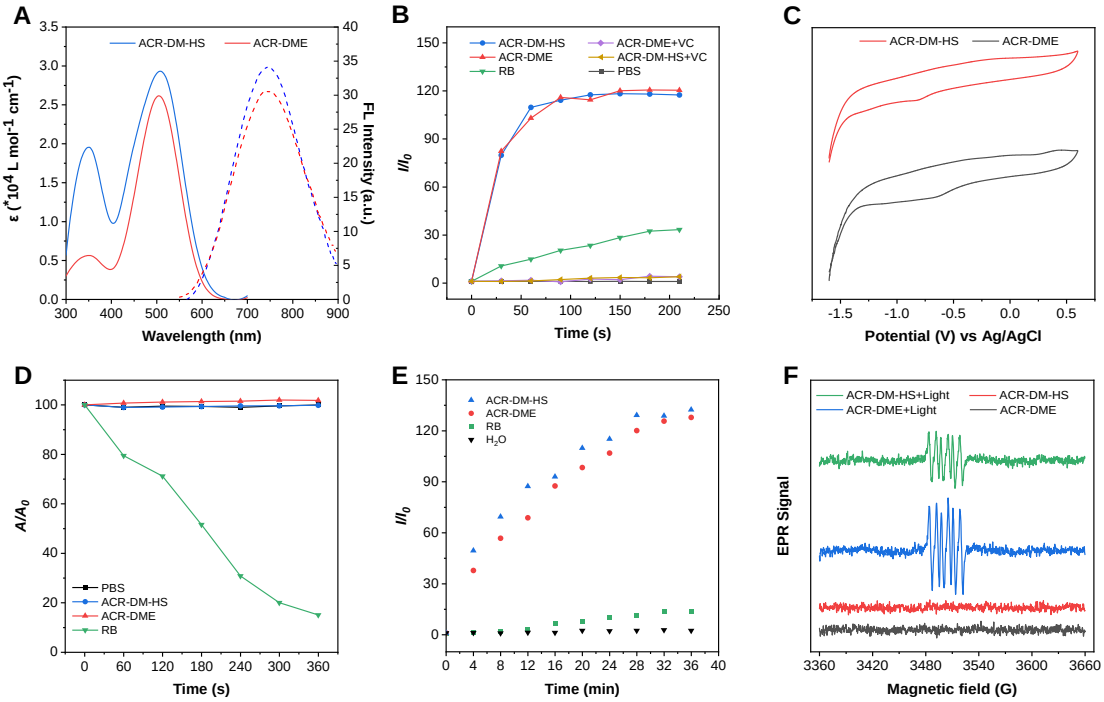

Figure 2. Photophysical properties of MMs (ACR-DM-HS and ACR-DME). (A) Molar absorption coefficients and photoluminescence spectra of MMs in DMSO solution. (B) ROS generation efficiency of MMs or RB upon white-light illumination. Relative changes in fluorescence intensity (I/I_0) of H_2DCF at 525 nm in the absence or presence of MMs with/without Vc in PBS under white light illumination at different time points. (C) Cyclic voltammogram of MMs in DCM with 0.1 M PBS as a supporting electrolyte, Ag/AgCl as a reference electrode, platinum-carbon compound electrode as a working electrode, Pt wire as a counter electrode and a scan rate of 20 mV s^{-1}. (D) Decomposition rates of ABDA in the absence or presence of MMs or RB under white light illumination. A_0 and A represented the initial and final absorbance of ABDA at 378 nm, respectively. (E) Determination of •OH generation ability of MMs upon white-light illumination. Relative changes in fluorescence intensity (I/I_0) at 515 nm of HPF in the absence or presence of MMs in water under white-light illumination at different time points. (F) EPR spectra of ROS generated by MMs upon white light irradiation using DMPO as a spin trapper.

Time-dependent density functional theory (TD-DFT) was employed to calculate three key parameters: (1) the absorption spectrum of the MMs, (2) the excited-state electron density distribution, and (3) the directional contributions of electric field components to both spectral features and charge density modulation.[13] As shown in Figure 1A and Figure S5, the spectral components were distributed along three principal axes: the transversal molecular plasmon resonance (red, dominant contribution), longitudinal (blue) and perpendicular (teal) axis. Figure 1D-1F illustrated the spatial distribution of total excited-state charge density in the ACR-DME and ACR-DM-HS systems under plasmon resonance conditions, with detailed axial decomposition revealing predominant contributions from the transverse component. Additionally, TD-DFT simulations revealed vibronic coupling effects through vibrationally-resolved absorption spectra (Figure 1B). Without nuclear vibrations, electronic transitions produce singular absorption peaks. In contrast, vibronic coupling enables transitions between the ground state and multiple vibrational sublevels in the excited state, generating characteristic second-order Franck-Condon progression peaks.[23] The dominant vibrational mode, visualized through vector projection analysis (Figure S6), primarily involved transverse molecular motions. Notably, the experimentally observed 510 nm shoulder (calculated as 565 nm by TD-DFT) represented the most intense vibronic feature among multiple coupled modes, demonstrating full-length molecular delocalization as evidenced by Supplementary Video S1 and S2. These computational findings established that photoexcitation of ACR-DM-HS and ACR-DME molecular plasmons induced coherent electron density oscillations that couple with nuclear vibrational modes through VDA mechanisms. This synergistic electron-nuclear dynamics ultimately drives membrane disassembly processes.

Resonance Raman spectroscopic analysis was performed to characterize vibrational dynamics (Figure 1C). The spectrum of ACR-DM-HS showed a prominent vibrational mode at 1431 cm^{-1} (period: 23.3 fs, frequency: 4.29×10^{13} Hz) corresponding to concerted molecular motions at terahertz frequencies (41 THz). Remarkably, these subpicosecond-scale coherent vibrations were 10^7-fold faster oscillatory dynamics than the megahertz-range (2-3 MHz) rotational cycles of Feringa-type motors (2016 Nobel Prize in Chemistry-winning rotary molecular machines).[14] Comparative analysis indicated that membrane rupture typically required 1-30 mN/m interfacial stress,[24] and cyanine-based molecular machines generated 26 mN/m interfacial stress within the critical range for membrane destabilization.[13] Spectroscopic measurements revealed a whole-molecule vibrational energy of 177.3 meV for ACR-DM-HS, corresponding to 0.028 nN directional force generation. This translated to 28 mN/m interfacial

10.1002/anie.202507833

stress, directly demonstrating membrane-disruptive capability through mechanochemical coupling.

Photophysical Property

The photophysical properties of MMs were investigated using UV-vis spectrophotometry and photoluminescence spectroscopy. These two MMs had a broad absorption spectrum ranging from 400 to 650 nm in dimethyl sulfoxide (DMSO), with an absorption maximum at around 510 nm and emission maximum at approximately 740 nm (Figure 2A).

To evaluate ROS generation efficiency, 2',7'-Dichlorodihydrofluorescein (H_2DCF) was used as an indicator, with Rose Bengal (RB) as a type II photosensitizer reference and vitamin C (Vc) as a ROS scavenger.[25,26] As shown in Figure 2B and Figure S7, the fluorescence intensity of H_2DCF hardly changed after 210 seconds of irradiation, whereas RB induced a 20-fold increase. Notably, ACR-DME and ACR-DM-HS produced significantly stronger fluorescence enhancements of 127-fold and 132-fold, respectively. By contrast, when Vc was added, no significant fluorescence increase was observed in the presence of either ACR-DME or ACR-DM-HS, demonstrating that they have exceptional ROS generation capacity, and VC can efficiently sweep away ROS generated by PDT of MMs.

The redox properties of the MMs were studied by cyclic voltammetry. As shown in Figure 2C, the ground-state reduction potentials of ACR-DME and ACR-DM-HS were -0.48 V and -0.59 V (*vs*. NHE), respectively, which were much lower than the reduction potential of O_2 to $O_2^{\bullet-}$ ($E(O_2 / O_2^{\bullet-})$ = -0.33 V *vs*. NHE).[27] This result indicates that ACR-DME and ACR-DM-HS may potentially produce type I ROS.

Subsequently, 9,10-anthracenediyl-bis(methylene)dimalonic acid (ABDA) was applied to assess the generation of singlet oxygen ($^1O_2$).[28] As shown in Figure 2D and Figure S8, the absorbance of ABDA at 378 nm kept consistently under white light irradiation for 0-360 seconds. However, with the addition of RB, the absorbance gradually decreased to 15.1% of its original value. On the contrary, ACR-DME or ACR-DM-HS barely decomposed ABDA. These results indicate that ACR-DME and ACR-DM-HS almost can not generate $^1O_2$ through type II mechanism.

For detection of hydroxyl radicals (•OH), hydroxyphenyl fluorescein (HPF) was employed.[29] HPF was mixed with the MM in water and then irradiated under white light. The fluorescence intensity at 515 nm was recorded (Figure 2E and Figure S9). After 36 minutes of illumination, ACR-DME and ACR-DM-HS increased the fluorescence intensity by 120-fold and 117-fold, respectively. In contrast, negligible fluorescence change was observed in the presence of RB.

Additionally, electron paramagnetic resonance (EPR) was employed to further analyze the ability of the MMs to produce free radicals using 5,5-dimethyl-1-pyrroline-N-oxide (DMPO) as the trapping agent.[30] As depicted in Figure 2F, illumination of the mixture of DMPO and ACR-DM-HS or ACR-DME, a sharp six-line EPR signal originating was detected. These results unequivocally demonstrate that both MMs efficiently produce type I ROS, enabling them to overcome the hypoxic microenvironment characteristic of biofilms.

Photo Induced Antibacterial Study

The antibacterial activities of the MMs were investigated. Gram-positive bacteria (G+), including *Staphylococcus aureus* (*S. aureus*) and Methicillin-resistant *Staphylococcus aureus* (MRSA), as well as the Gram-negative bacteria (G-) *Escherichia coli* (*E. coli*), were selected for evaluation. The bacteria were incubated with different concentrations of ACR-DM-HS or ACR-DME for 10 minutes, followed by either 30 minutes of white light irradiation or dark conditions. The antibacterial effects were assessed using a plate counting method. As shown in Figure 3A-3F and Figure S10, both ACR-DM-HS and ACR-DME exhibited minimal dark toxicity against G+ and G−, with survival rates exceeding 90% for *S. aureus*, MRSA, and *E. coli* even after treatment with 10 μM ACR-DME or ACR-DM-HS. However, under light irradiation, ACR-DME demonstrated potent bactericidal activity against G+. Increasing the concentration from 2.5 μM to 10 μM led to a dramatic reduction in the survival rates of *S. aureus* from 68.9% to 1.0% (Figure 3A) and MRSA from 50% to virtually 0% (Figure 3B). In contrast, *E. coli* showed no significant decrease in survival rate (Figure 3C). Notably, ACR-DM-HS showed significantly stronger antibacterial effects than ACR-DME against both G+ and G−. More than 98% *S. aureus*, 99.9% MRSA, and 90% *E. coli* were eradicated when treated with 5 μM ACR-DM-HS (Figure 3D-3F). Furthermore, the minimum inhibitory concentration (MIC) values of ACR-DM-HS were determined to be 2.5 μM for MRSA and 10 μM for *E. coli* (Figure S11).

Vc was added to investigate the contribution of VDA and PDT to the antibacterial activity. Strikingly, despite the presence of a 100-fold molar excess of Vc (which completely scavenges ROS in solution, as confirmed in Figure 2B and Figure S7), both ACR-DM-HS and ACR-DME maintained bactericidal activity. ACR-DME exerted VDA-mediated killing against 38.9% of *S. aureus* and 50.6% of MRSA (Figures 3A-3C). Notably, ACR-DM-HS exhibited stronger VDA effects, eliminating 50.5% of *S. aureus*, 57.8% of MRSA, and 52.6% of *E. coli* (Figures 3D-3F).

Furthermore, bacterial morphology was examined using scanning electron microscopy (SEM). As shown in Figure 3G and Figure S12, both MRSA and *E. coli* retained intact spherical or rodlike structures when exposed to ACR-DM-HS or ACR-DME in the dark. However, upon light irradiation, both MMs induced significant morphological alterations in MRSA, including cell wall distortion, membrane collapse, intercellular fusion, and cytoplasmic hollowing, even in the presence of Vc. Notably, only ACR-DM-HS caused membrane fusion and collapse effects on *E. coli* under these conditions.

Subsequent ultrastructural analysis by transmission electron microscopy (TEM) was performed to investigate VDA-induced membrane perturbations. As revealed in Figure 3H, marked morphological disparities were observed. Untreated MRSA cells maintained characteristic turgidity with well-preserved ultrastructure, including intact membranes and densely packed cytoplasmic compartments. By contrast, ACR-DM-HS +Vc +Light group (VDA-only condition) pronounced membrane discontinuities accompanied by cytoplasmic efflux. Most strikingly, the ACR-DM-HS + Light group (combined VDA+ROS action) demonstrated aggravated membrane damage, characterized by simultaneous disruption of both cell wall integrity and plasma

10.1002/anie.202507833

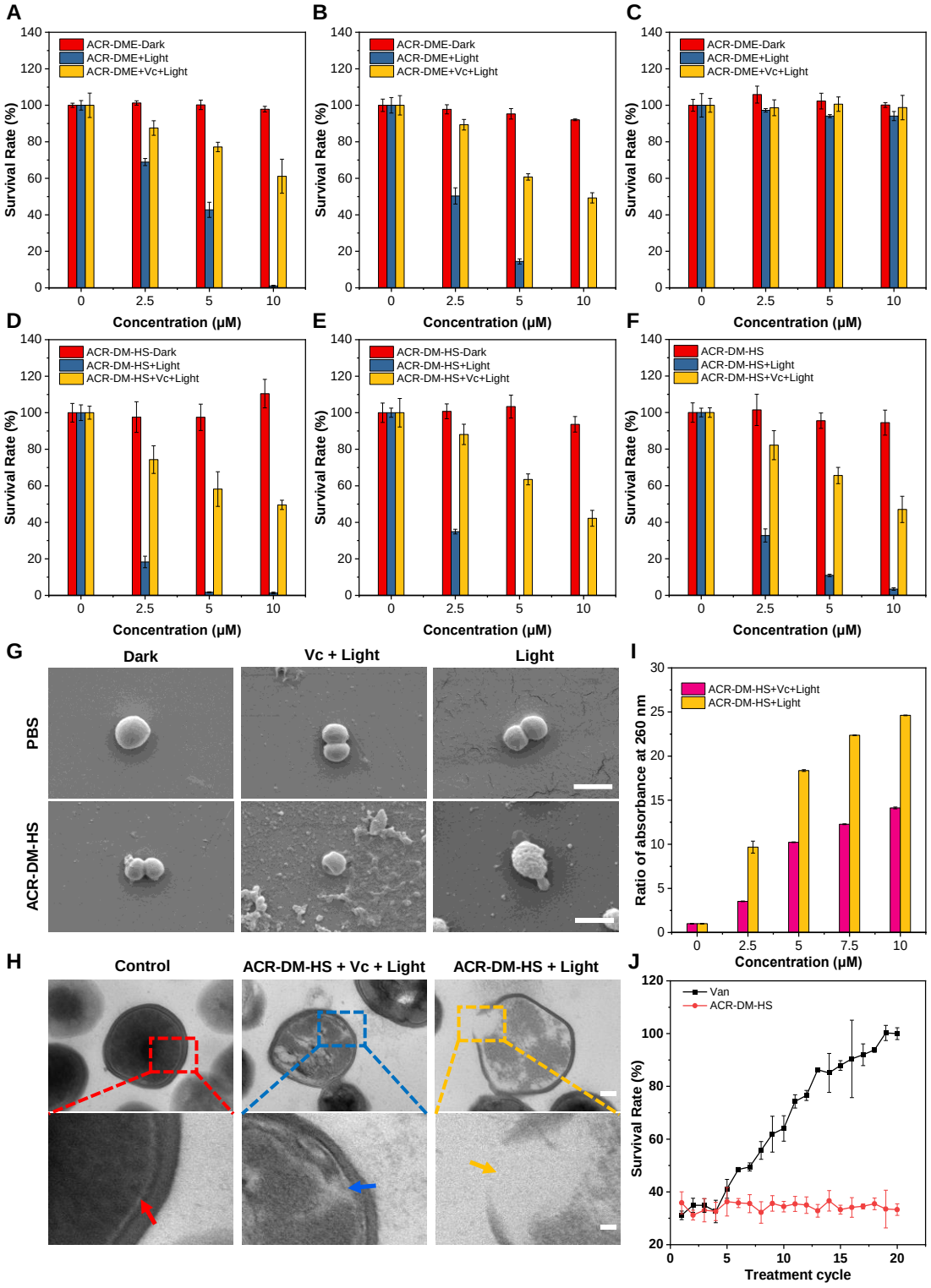

Figure 3. Antibacterial activity of MMs against *S. aureus* (A, D), MRSA (B, E), and *E. coli* (C, F). Bacteria were treated with different concentrations of ACR-DME (A, B, C) or ACR-DM-HS (D, E, F), followed by either kept in the dark or exposed to white light in the absent or present of Vc. SEM images (G) and TEM images (H) of MRSA with different treatment. Scale bars: SEM-1 μm; TEM-100 nm (top), 25 nm (bottom). The red arrow indicates the intact bacterial plasma membrane, the blue arrow points to the damaged bacterial plasma membrane, and the yellow arrow denotes the damaged bacterial cytoplasmic and cell wall. (I) UV absorbance ratio at 260 nm of the supernatant from MRSA after incubated with ACR-DM-HS under dark or white light in the absence or presence of Vc. (J) Drug susceptibility test of MRSA to vancomycin (20 μM) and ACR-DM-HS (2.5 μM). MRSA was incubated with vancomycin for 12 hours, or ACR-DM-HS for 10 minutes followed by 30 minutes of white light irradiation. Bacterial survival was assessed by plate colony counting. A single colony was selected from the plate where the bacteria survived at the highest drug concentration to continue the culture. The bacterial survival rate was recorded for 20 consecutive cycles of treatment. The data were presented as the means ± SDs (n = 3).

10.1002/anie.202507833

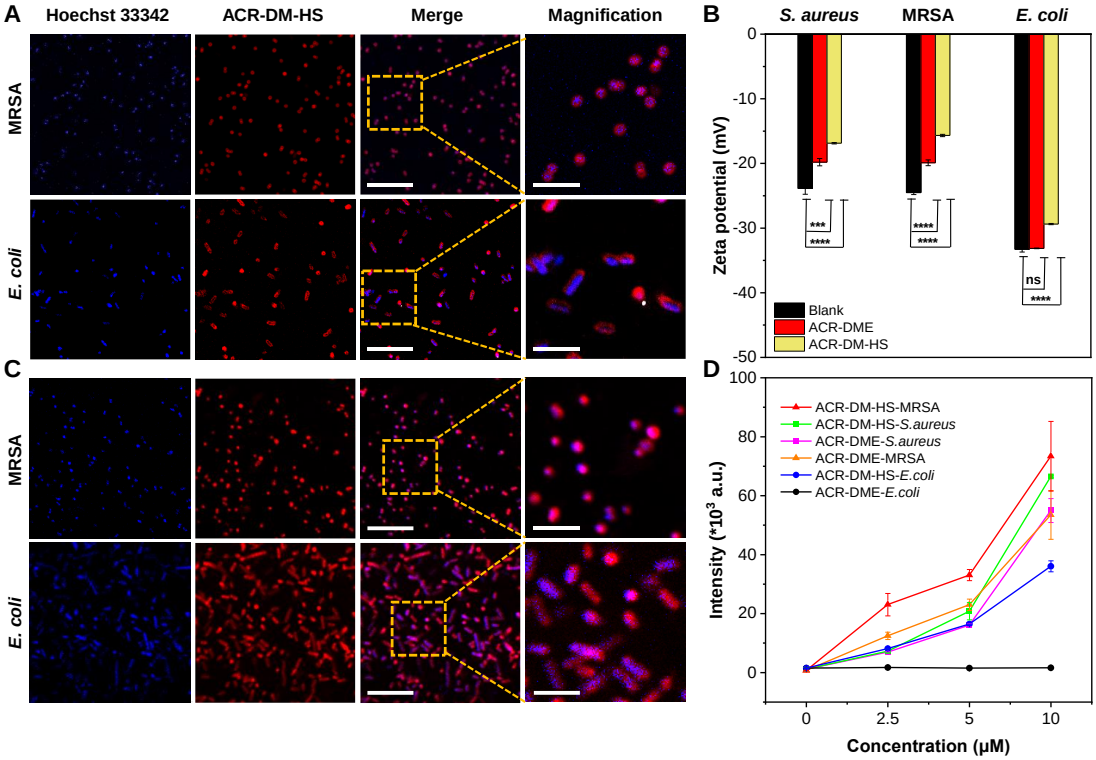

Figure 4. The binding ability of MM with different kinds of bacteria. (A) Fluorescence images of MRSA and *E. coli* co-incubated with 10 μM of ACR-DM-HS and 20 μM Hoechst 33342. ACR-DM-HS: λ_{ex} = 561 nm, λ_{em} = 650-750 nm. Hoechst 33342: λ_{ex} = 405 nm, λ_{em} = 430-480 nm. Scale bars: 10 μm. Magnification scale bars: 3 μm. (B) ζ changes of *S. aureus*, MRSA, and *E. coli* incubated with different MM. (C) Fluorescence images of MRSA and *E. coli* pretreated with Vc (1000 μM), incubated with 10 μM of ACR-DM-HS for 10 minutes and illuminated with light for 30 minutes. Scale bars: 10 μm. Magnification scale bars: 3 μm. (D) Flow cytometry analysis of the permeability of MM to different kinds of bacteria. The data were presented as the means ± SDs (n = 3) and were analyzed by one-way ANOVA with GraphPad Prism software. ns means no significance; ***p < 0.001; ****p < 0.0001.

membrane continuity, resulting in complete cytoplasmic depletion. This comparative ultrastructural analysis reveals that VDA independently compromises membrane integrity, while additional ROS activation triggers catastrophic cellular decompartmentalization. Consistent with these observations, fluorometric quantification revealed dose-dependent elevation of cytoplasmic constituent (e.g., nucleic acids) leakage in both treatment groups, providing quantitative validation of membrane permeabilization efficacy (Figure 3I). [31]

Long-term antimicrobial resistance (AMR) development potential under chronic exposure conditions was systematically evaluated for ACR-DM-HS. MRSA were subjected to 20-cycle serial passaging with either vancomycin or ACR-DM-HS combined with light treatment (Figure 3J and Figure S13-S16). Initial vancomycin exposure (20 μM) eradicated 69% of the initial population, but serial passaging induced complete resistance development, manifested as 100% survival by cycle 20. In marked contrast, ACR-DM-HS+L (2.5 μM) maintained consistent antimicrobial efficacy across 20 treatment cycles, achieving sustained ~65% growth inhibition without any loss of potency. This longitudinal analysis conclusively demonstrates the absence of detectable resistance evolution against ACR-DM-HS's treatment, which may stem from the synergistic combination of physical membrane disruption and ROS-mediated biochemical attack antimicrobial strategy that precludes conventional resistance pathways—bacteria may develop resistance to conventional PDT by downregulating oxidative stress responses, particularly in the hypoxic and glutathione-enriched microenvironment of biofilm infections.[32]

Investigation the Antibacterial Mechanism

To investigate the binding affinity of these MMs with different types of bacteria, fluorescence imaging was employed. MRSA and *E. coli* were incubated with 10 μM ACR-DM-HS or ACR-DME for 10 minutes, and then counterstained with 20 μM Hoechst 33342 for 20 minutes. The fluorescence images were captured using confocal laser scanning microscopy (CLSM). As illustrated in Figure 4A and Figure S17, both MRSA and *E. coli* showed distinct fluorescent signals after ACR-DM-HS staining. In contrast, ACR-DME displayed selective binding to MRSA, as evidenced by its specific fluorescence. In the magnified images, the ACR-DM-HS staining clearly outlined the MRSA or *E. coli* contours, complementing the fluorescence of protoplasmic DNA stained by Hoechst 33342. These results demonstrate that ACR-DME selectively binds to G+ cytoplasmic membranes, while ACR-DM-HS exhibits binding affinity for both G+ and G- cytoplasmic membranes.

The zeta-potential (ζ) analysis of the bacterial surface was performed to assess the binding ability of the MMs. As illustrated in Figure 4B, the ζ values of *S. aureus*, MRSA, or *E. coli* was -23.8, -24.5, or -33.2 mV, respectively. Following incubation with

10.1002/anie.202507833

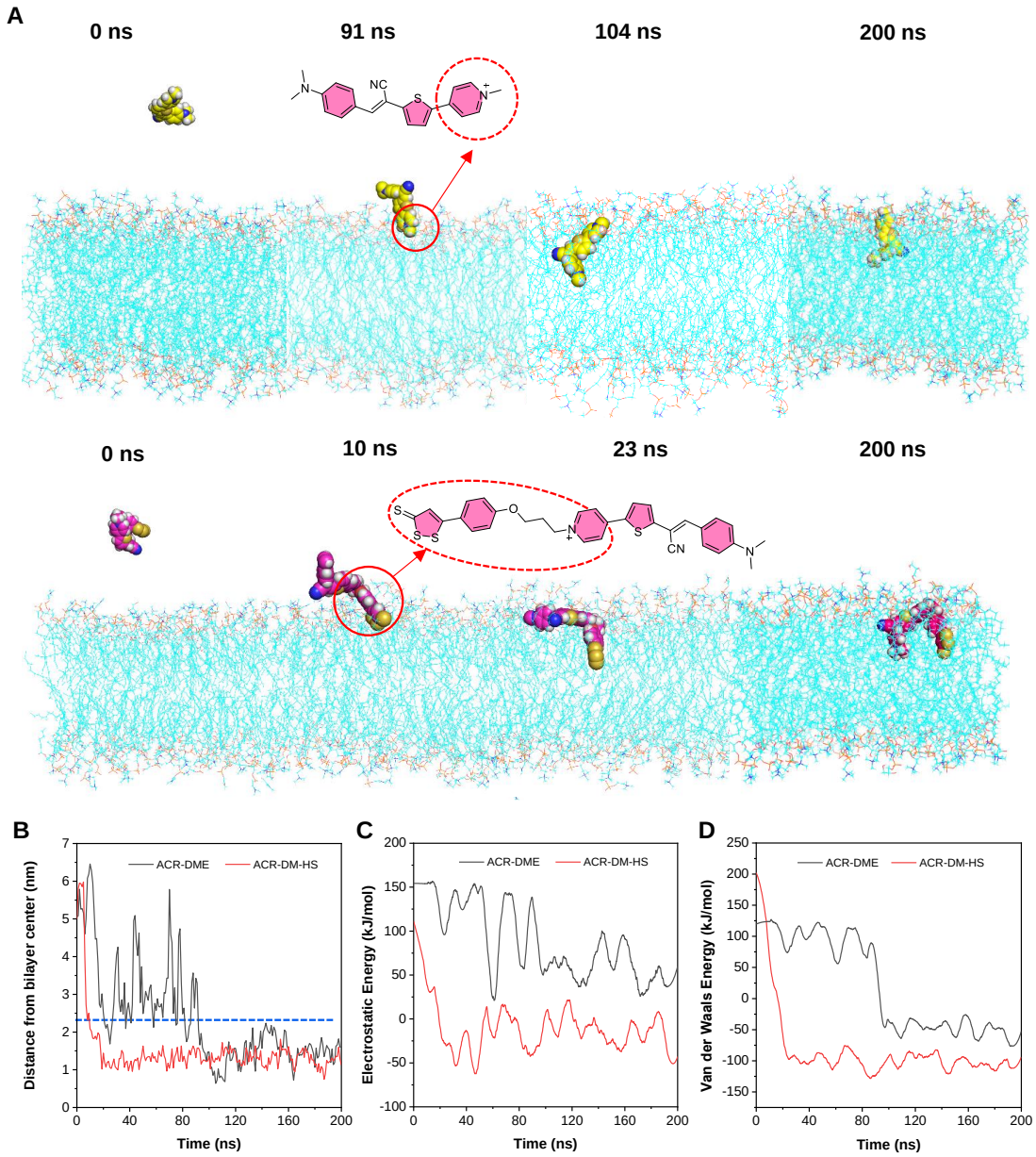

Figure 5. The interaction of MM with membrane phospholipid bilayers. (A) Simulated configurations of MMs interacting with the membrane of MRSA (DOPC: DOPG= 7:3), including initial attachment, penetration, and equilibrium embedding. (B) The representative temporal evolution of the COM distance between MM and the lipid bilayer throughout the simulated interaction process. The dot-dashed blue lines in (B) represent the surface of the membrane. Interaction energies between MM and membrane phospholipid bilayer: (C) electrostatic interactions and (D) van der Waals interactions.

5 μM ACR-DME, the ζ of *S. aureus* or MRSA were partially neutralized to -19.8 or -19.9 mV, respectively. However, ACR-DME can hardly change the ζ of *E. coli*. Strikingly, ACR-DM-HS increased the negative potential of *S. aureus* to -15.7 mV, MRSA to -16.9 mV, and *E. coli* to -29.4 mV. demonstrating its strong binding affinity to both G+ and G-.

To investigate the damage to bacterial plasma membranes caused by the VDA of the MMs, the bacteria were incubated with 10 μM MM for 10 minutes and then irradiated with white light in the presence of Vc for an additional 30 minutes. Subsequently, the bacteria were stained with Hoechst 33342 for20 minutes, and fluorescence imaging was performed. As shown in Figure 4C and Figure S18, both ACR-DM-HS and ACR-DME penetrated the plasma membrane of MRSA and distributed throughout the bacterial cells. Meanwhile, a fluorescence signal was observed in the *E. coli* only after treated with ACR-DM-HS. Sytox Green is a commercial probe that can only penetrate damaged bacterial cell membranes to stain the nucleic acids.[33] Vc treated bacteria were incubated with 10 μM MM for 10 minutes, exposed to white light for 30 minutes, and then stained with Sytox Green for 20 minutes. As shown in Figure S19, ACR-DM-HS and ACR-DME compromised the plasma membrane to turn on all the bacteria and kill the MRSA, and the nuclei were lit up by Sytox Green. Nevertheless, only ACR-DM-HS disrupted the plasma membrane

10.1002/anie.202507833

of *E. coli,* leading to green fluorescence of Sytox Green. Additionally, fluorescence intensity was quantified by flow cytometry to assess the effect of VDA on bacterial membrane permeability. As shown in Figure 4D, upon treatment with ACR-DME, the fluorescence intensity in *S. aureus* and MRSA increased significantly with increasing concentration, whereas the fluorescence intensity of *E. coli* remained unchanged. In contrast, markedly enhanced fluorescence intensity from ACR-DM-HS was observed in *S. aureus*, MRSA and *E. coli*. These results indicate that ACR-DM-HS disrupts the integrity of the plasma membrane and alter the permeability of both G+ and G- through VDA, while ACR-DME selectively disrupts the plasma membrane of G+.

Molecular Dynamics (MD) Simulations of MM Membrane Interactions

We conducted an in-depth investigation into the interactions between MM and the plasma membrane at the molecular level using all-atom MD simulations. The *S. aureus* bacterial membrane lipid bilayer model was constructed with dioleoyl-sn-glycero-3-phosphocholine (DOPC) and 1,2-dioleoyl-sn-glycero-3-phospho-(1'-rac-glycerol) (DOPG) in a ratio of 7:3.[34] MD simulations revealed that ACR-DME was initially recruited to the lipid membrane surface at 91 ns due to the binding of its polar regions, such as pyridinium, with the hydrophilic heads of lipids via polar and electrostatic interactions (Figure 5A). After 13 ns of continuous attachment, ACR-DME penetrated the membrane and embedded into the lipid bilayer in an "L" shape, maximizing interactions between nonpolar dimethyl aniline, double bond, thiophene with hydrophobic lipid tails. Notably, as soon as 10 ns, ACR-DM-HS bound to the polar region via 1,2-dithiole-3-thione and pyridinium, which was nearly nine times faster than ACR-DME. After 13 ns of sustained attachment, it successfully entered the membrane and eventually adopted a "Π" configuration with 1,2-dithiole-3-thione, dimethyl aniline, double bond and thiophene inserting into hydrophobic lipid through hydrophobic interaction and pyridinium interreact with hydrophilic heads through polar and electrostatic interactions, firmly anchoring itself to the membrane. This embedded configuration remained stable throughout the rest of the simulation as showed by temporal evolution of the center of mass (COM) distance between ACR-DM-HS and the lipid bilayer (Figure 5B).

Furthermore, the interaction of MM with the membrane was evaluated. A more negative value indicates a higher propensity to form a stable combination.[35] As shown in Figure 5C-5D, when ACR-DME or ACR-DM-HS combined with the membrane at 104 ns or 23 ns, respectively, the electrostatic interaction between them showed a certain level of stability. The electrostatic energy values in the membrane system were recorded as -58.0 kJ/mol for ACR-DM-HS and +26.6 kJ/mol for ACR-DME. In addition, the van der Waals in the membrane system was -112.7 kJ/mol for ACR-DM-HS or -63.3 kJ/mol for ACR-DME, respectively. Compared with ACR-DME, ACR-DM-HS has lower electrostatic interaction energy and van der Waals when binding to the membrane, indicating that ACR-DM-HS is more likely to bind with the membrane and integrate into the membrane in a stable "Π" structure. Therefore, ACR-DM-HS demonstrated stronger antibacterial activity.

In Vitro Eradication of Biofilms

Compared to planktonic bacteria, biofilms offer much stronger protection through extracellular polymeric substance to prevent antibiotic permeation, making them much more resistant to antibiotics for 10-1000 fold.[36] The potential of MMs to eradicate biofilms was investigated. The crystal violet staining method was initially used to quantify the biofilm biomass. As illustrated in Figure 6A, biofilms of *S. aureus*, MRSA, and *E. coli* were successfully stained with crystal violet, resulting in a distinct dark blue color. When only treated with 20 μM of ACR-DM-HS or ACR-DME, the biofilm remained unchanged. However, upon light irradiation, both ACR-DME and ACR-DM-HS efficiently eradicated *S. aureus* and MRSA biofilms. Notably, only ACR-DM-HS was able to remove the *E. coli* biofilms. To further quantify the remaining biofilm, the optical density (OD) of the crystal violet-stained biomass was measured using a microplate reader.[37] As shown in Figures 6B-6D, neither ACR-DME nor ACR-DM-HS had a negligible impact on the biofilm biomass in the absence of light. However, under white light irradiation, ACR-DME and ACR-DM-HS demonstrated dose-dependent antibiofilm activity against *S. aureus* and MRSA. 20 μM ACR-DME removed 85% *S. aureus* or 95% MRSA biofilm biomass. In comparison, ACR-DM-HS eliminated 93% *S. aureus*, 99% MRSA or 90% *E. coli* biofilm biomass under the same condition.

Moreover, 3D fluorescence images of MRSA and *E. coli* biofilms were investigated using CLSM. Sytox Green was employed to detect dead bacteria within the biofilms. As depicted in Figure 6E-6F, only red fluorescence signals were observed in the MRSA biofilms treated with either ACR-DME or ACR-DM-HS. Upon subsequent light irradiation, the MRSA biofilm exhibited Sytox Green fluorescence after treatment with either ACR-DME or ACR-DM-HS. Nevertheless, *E. coli* biofilms were stained exclusively by ACR-DM-HS, which subsequently showed Sytox Green fluorescence upon light irradiation.

Meanwhile, the morphological analyses were carried out by SEM (Figure 6G-6H). In both the control and dark groups, the bacteria had regular shapes, smooth surfaces, and intact cell membrane. After treatment with ACR-DM-HS, pronounced membrane folds, collapses and membrane fusion of MRSA and *E. coli* were observed under light exposure. This phenomenon was similarly observed on ACR-DME-treated MRSA biofilms. These results demonstrate that ACR-DM-HS effectively eradicates G+ and G- biofilms and kills the bacteria inside, while ACR-DME is effective only against G+ biofilm.

The Anti-inflammatory Activity and Angiogenic Potential of ACR-DM-HS

Currently, most reported H_2S donors are activated by biothiols, which indiscriminately released H_2S in both bacteria or eukaryocyte, weakening the antibacterial activity by ROS.[18] In comparison, ADT-OH releases H_2S in response to mitochondrial enzymes,[38] which can effectively avoid the mutual interference between ROS and H_2S by releasing H_2S exclusively in eukaryocyte. We detected the release of H_2S from ACR-DM-HS in MRSA and human umbilical vein endothelial cells (HUVECs) using the H_2S fluorescent probe Washington State Probe-5 (WSP-5) (Figure S20).[39] The MRSA treated with ACR-DM-HS or

10.1002/anie.202507833

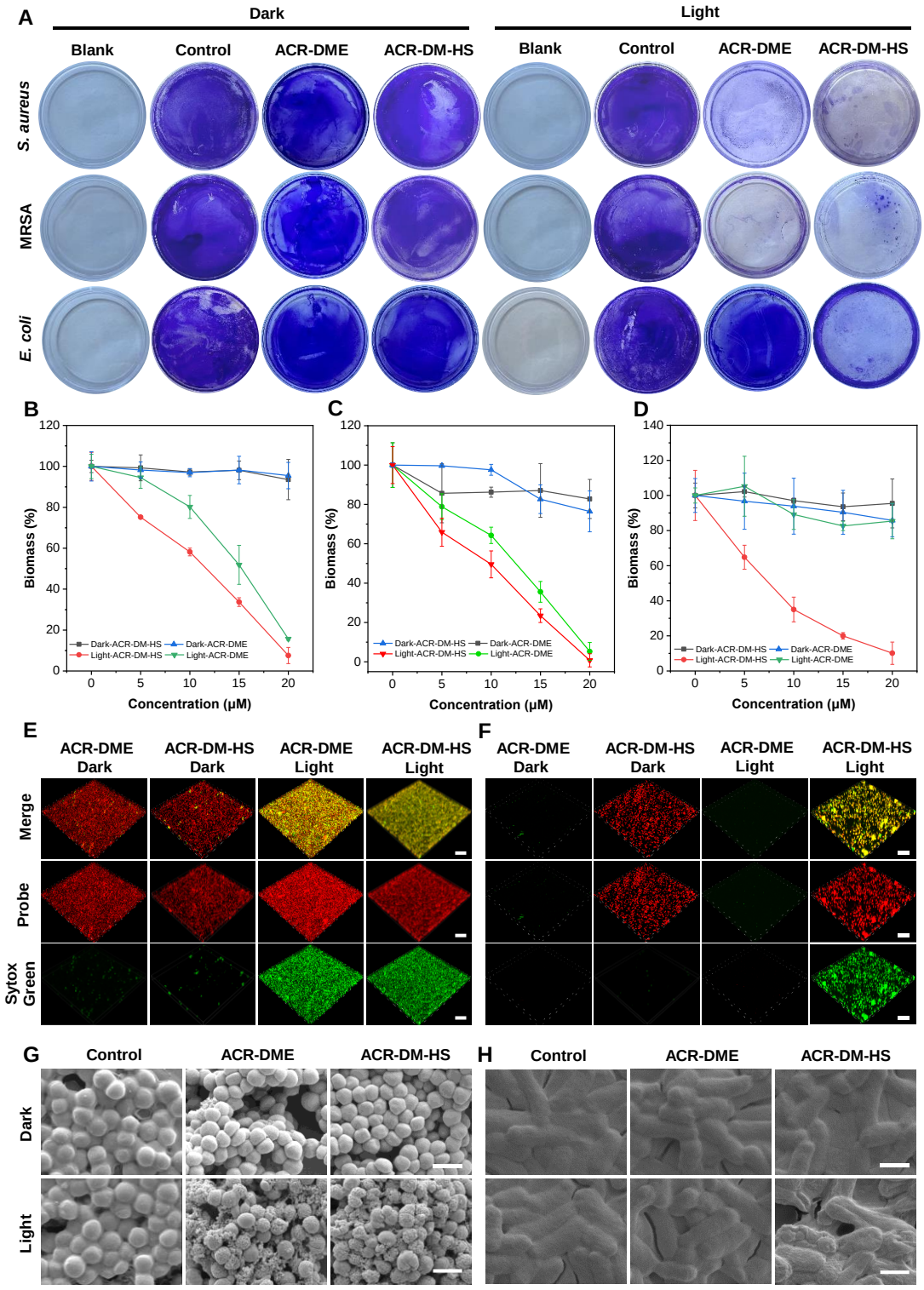

Figure 6. Antibiofilm activity of MMs. (A) Images of *S. aureus*, MRSA and *E. coli* biofilms stained with crystal violet on culture dishes. Quantitative analysis of residual biofilm biomass for *S. aureus* (B), MRSA (C), and *E. coli* (D) after treatment with MMs, either kept in the dark or exposed to white-light irradiation. Representative 3D images of MRSA (E) and *E. coli* (F) biofilms treated with ACR-DME or ACR-DM-HS, either kept in the dark or exposed to white-light illumination. Scale bars: 20 μm. SEM images of MRSA (G) and *E. coli* (H) biofilms after different treatment to analyze morphology changes. Scale bars: 1 μm. The data were presented as the means ± SDs (n = 3).

ADT-OH showed negligible fluorescence. This may be attributed to the absence of the corresponding mitochondrial enzymes in bacteria. In contrast, HUVECs exhibited strong green fluorescence following treatment with ADT-OH or ACR-DM-HS.

10.1002/anie.202507833

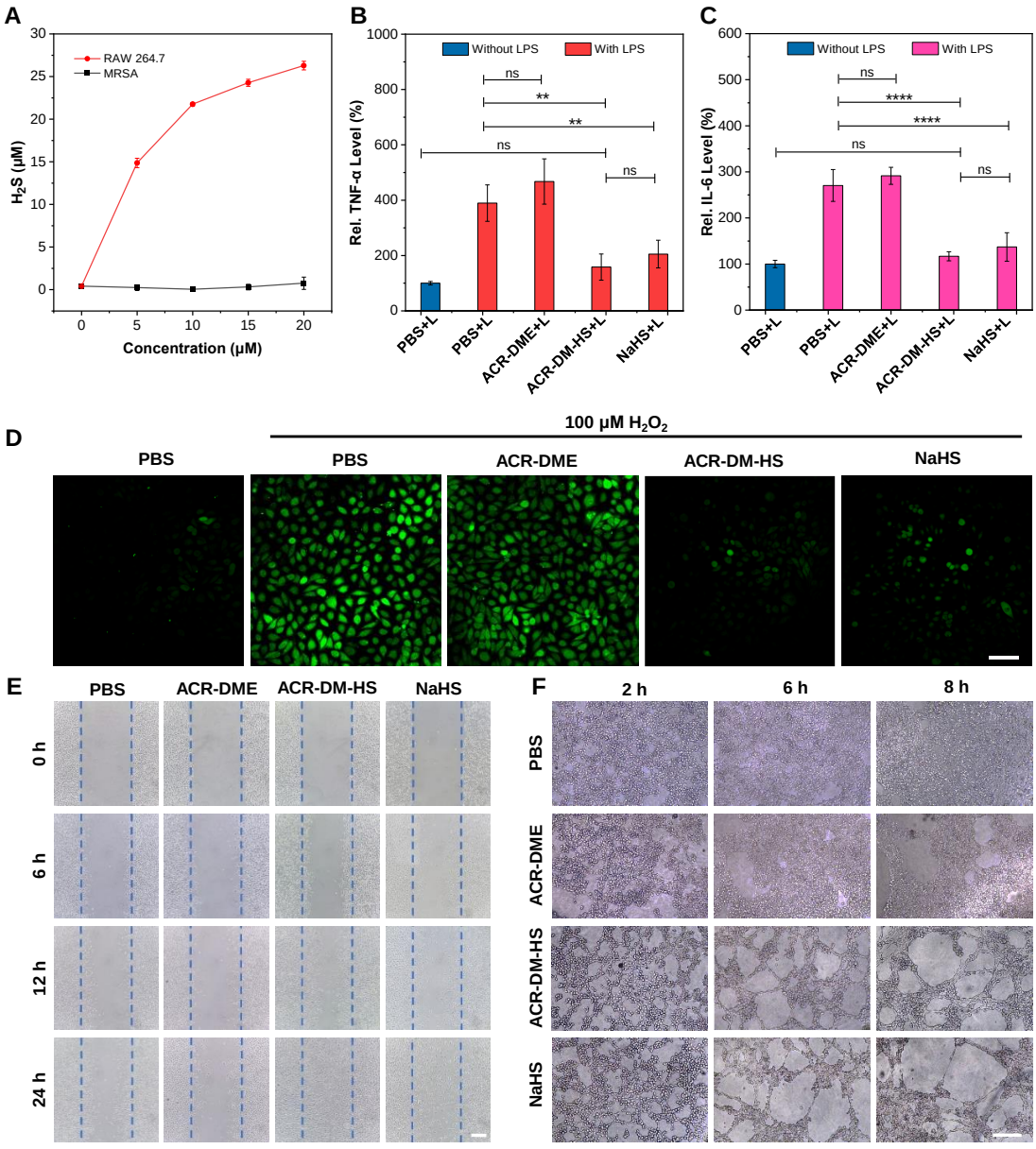

Figure 7. H_2S release ability, ROS elimination, anti-inflammation, cell proliferation and angiogenesis performance of ACR-DM-HS. (A) Quantitative determination of H_2S release in RAW 264.7 cell lysate or MRSA lysate with different concentrations of ACR-DM-HS. Expression of inflammatory cytokines TNF-α (B) and IL-6 (C) in LPS-pretreated RAW264.7 cells. (D) The fluorescence images of ROS in H_2O_2 pretreatment HUVECs cells with different treatment. ROS was probed by H_2DCF (E) Cell scratch migration analysis of L929 cells treated with ACR-DME, ACR-DM-HS or NaHS. Scale bar: 100 μm. (F) Angiogenesis ability of HUVECs treated with ACR-DME, ACR-DM-HS or NaHS. Scale bar: 100 μm. The data were presented as the means ± SDs (n = 3) and were analyzed by one-way ANOVA with GraphPad Prism software. ns means no significance; **p < 0.01; ****p < 0.0001.

Besides, ACR-DM-HS was added to macrophage lysate or MRSA lysate, and H_2S release was detected using a commercial kit. As shown in Figure 7A, MRSA lysate failed to promoted the H_2S release. However, in the presence of macrophage lysate, H_2S gradually increased with the ACR-DM-HS concentration increasing. These results confirm that ACR-DM-HS can selectively release H_2S in mammalian cells.

The biocompatibility of ACR-DME and ACR-DM-HS was evaluated by haemolysis test. As shown in Figure S21, under light conditions, even at the concentration of 20 μM, the hemolysis rate of ACR-DME or ACR-DM-HS was lower than 5%.

In addition, the Cell Counting Kit-8 (CCK-8) assay was employed to evaluate the cytotoxicity of MMs. HUVECs were incubated with different concentrations of MM, and then either kept in darkness or exposed to light. As shown in the Figure S22, the cell viability of HUVECs treated with ACR-DME remained above 90% regardless of dark or light conditions. Interestingly, after incubation with 20 μM ACR-DM-HS, the survival rate of HUVECs was as high as 130.1%. Even under light irradiation, the survival rate exceeded 120%, suggesting that ACR-DM-HS may promote cell proliferation via H_2S release.

10.1002/anie.202507833

Moreover, CLSM was used to evaluate the selective antibacterial activity of MRSA by ACR-DM-HS. Following incubation of MRSA or HUVECs with ACR-DM-HS (10 μM) for 1 h, fluorescence images were recorded. As shown in Figure S23, MRSA exhibited strong red fluorescence from ACR-DM-HS. Nevertheless, it can hardly turn on HUVECs. This is due to the more negative membrane potential of bacteria compared with eukaryotic cells. Furthermore, HUVECs cells were co-cultured with MRSA and incubated with 10 μM ACR-DM-HS for 30 min, followed by white light irradiation for 30 min, and then stained with Sytox Green. As shown in Figure S24, only MRSA was simultaneously illuminated by ACR-DM-HS and Sytox Green, while no fluorescence was observed in HUVECs. These findings indicate that ACR-DM-HS can selectively kill MRSA without compromising mammalian cell viability.

The ROS-overexpression in diabetic wound was the major factor compromising cell proliferation, migration, and vascularization, resulting in slow wound healing.[40] HUVECs play an essential role in angiogenesis. An oxidative stress model of HUVECs induced by hydrogen peroxide (H_2O_2) was further established.[41] Subsequently, the cells were treated with ACR-DME, ACR-DM-HS, or NaHS (a widely used H_2S releaser), and then incubated with H_2DCF solution to detect intracellular ROS. As shown in Figure 7D, H_2O_2 irritative cells had much higher level of ROS. After further treated with ACR-DME, the ROS production level in the cells remained unchanged, and strong green fluorescence was still observed. In contrast, ACR-DM-HS significantly reduced the green fluorescence, achieving a similar ROS-scavenging effect to that of NaHS. These results suggest that ACR-DM-HS can effectively scavenge ROS and reduce intracellular oxidative stress through H_2S release.

Sustained inflammatory responses in chronic wounds impede the formation of new blood vessels and collagen deposition.[42] H_2S has been shown to inhibit the production of inflammatory cytokines, thereby exerting an anti-inflammatory effect in the cellular microenvironment.[43] Therefore, we aimed to harness the specific H_2S-releasing capacity of ACR-DM-HS to mitigate inflammation. Tumor necrosis factor-α (TNF-α) and interleukin-6 (IL-6) are key inflammatory mediators that are significantly elevated in chronic wounds. The overexpression of TNF-α and IL-6 can induce a persistent inflammatory state, leading to delayed wound healing. LPS-pretreated RAW264.7 cells were incubated with ACR-DME, ACR-DM-HS or NaHS, and then irradiated with light. TNF-α and IL-6 levels were quantified via ELISA. As illustrated in Figure 7B-7C, compared with the control group, TNF-α and IL-6 levels in both the LPS group and ACR-DME group were significantly elevated. Nevertheless, both ACR-DM-HS and NaHS could reduce the TNF-α and IL-6 to normal levels, which were similar to the control group, indicating that ACR-DM-HS has excellent anti-inflammatory properties.

Angiogenesis is closely related to the cellular proliferation and migration. Scratch assays were conducted to investigate cell growth and proliferation promoted by ACR-DM-HS. As shown in Figure 7E and Figure S25, treatment with ACR-DM-HS or NaHS for 24 hours resulted in significantly enhanced cell proliferation, with complete (100%) scratch closure. However, there were only 48.4% coverage for control group, 46.3% for ACR-DME group. Besides, the angiogenesis-promoting capability of ACR-DM-HS was further validated through a Matrigel-based angiogenesis experiment. As illustrated in Figure 7F, both the ACR-DM-HS and NaHS groups exhibited early vascular structure formation within 2 hours of incubation, developed a robust tubular network by 6 hours, and achieved fully mature structures by 8 hours. No such angiogenic activity was detected in the control or ACR-DME groups. These findings demonstrate that ACR-DM-HS effectively stimulates cellular proliferation and potently induces angiogenesis.

In Vivo Therapy of Chronic Diabetic Wound

Based on the excellent antibacterial and anti-inflammatory properties of ACR-DM-HS, we further investigated its application *in vivo* for MRSA-infected diabetic wounds (Figure 8A). A diabetic mouse model was successfully established via intraperitoneal injection of streptozotocin, with blood glucose levels consistently maintained above 16.7 mmol/L throughout the study period. Subsequently, 10-mm diameter full-thickness skin wounds were created and infected with MRSA, then randomly divided into five treatment groups: treated with PBS (control group), treated with ACR-DM-HS (ACR-DM-HS group), treated with vancomycin (Van group), ACR-DME-mediated PDT (ACR-DME+L group), and ACR-DM-HS mediated synergistic antibacteria and anti-inflammation alleviation therapy (ACR-DM-HS+L group).

Wound healing progression was monitored over 12 days (Figure 8B and Figure S26). In the control group, wounds exhibited visible signs of infection by day 1, progressing to severe purulent inflammation by day 3. Spontaneous healing initiated by day 7 through host immune responses resulted in a mean wound area of 27.9 mm^2 by day 12. The ACR-DM-HS group displayed comparable infection severity to control group from day 1 to day 7, achieving a 19.7 mm^2 wound area by day 12. Although H_2S has anti-inflammatory and angiogenic properties, its release from ACR-DM-HS alone was insufficient for complete wound healing due to persistent bacterial infection in diabetic wounds. However, Van can efficiently kill the bacteria and reduce the purulence with wound healing beginning on day 3, leaving a wound area of 3.8 mm^2 by day 12. Meanwhile, mice treated with ACR-DME under light showed a certain degree of suppuration on the third day, progressing to a 12.8 mm^2 wound area by day 12. This improvement was attributed to the capacity of ACR-DME to eradicate pathogenic bacteria via VDA and PDT under white light irradiation, thereby reducing the microbial burden in chronic wounds to accelerate wound healing. Most remarkably, in the ACR-DM-HS+L group, mice demonstrated minimal infection on day 1 with consistent healing throughout the study, leading to imperceptible scarring by day 12. The ACR-DM-HS-mediated comprehensive therapy greatly promoted the wound healing. This was attributed to H_2S release from ACR-DM-HS, which effectively reduced inflammatory cytokine expression and promoted angiogenesis after killing the MRSA through VDA and PDT in the wound tissues. Thus, the combined antibacterial, anti-inflammatory, and angiogenic effects collaboratively facilitated wound healing.

The therapeutic efficacy was further assessed by counting the colony numbers on the LB agar plates from homogenized wound tissue samples (Figure 8C and Figure S27). In MRSA infected mice treated with PBS or ACR-DM-HS alone, there was bacterial

10.1002/anie.202507833

RESEARCH ARTICLE

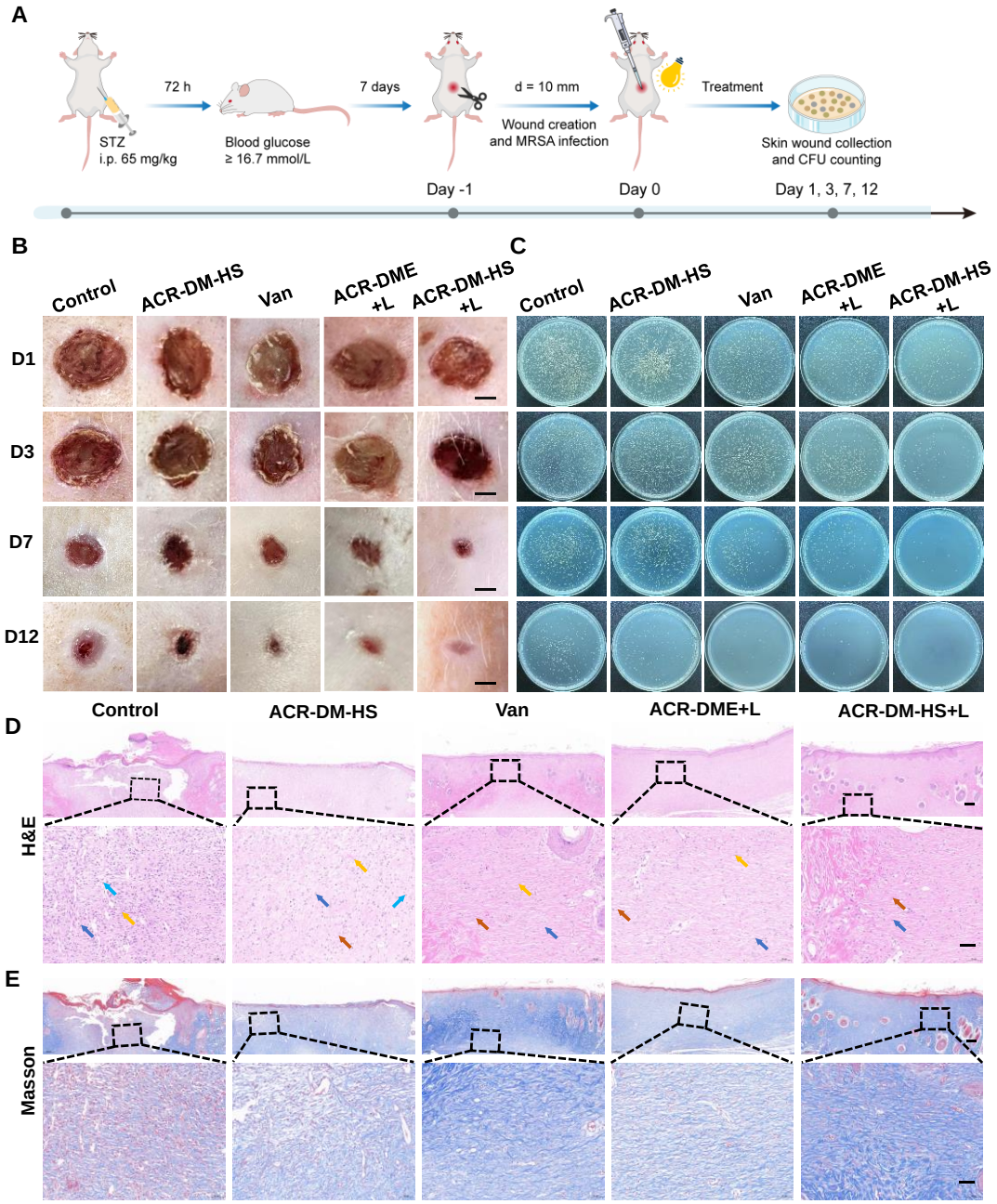

Figure 8. *In vivo* therapy of MRSA-infected diabetic wound. (A) Schematic representation of the *in vivo* experiment for MRSA-infected diabetic wound. (B) Photographs of wound healing of MRSA-infected diabetic rats with 12 days different treatments, scale bars: 2.5 mm. (C) Images of bacterial colonies in wound tissue with different treatments. (D) H&E staining images of wounds in rats from each group on day 12. Different colored arrows highlight the pathology of the wound: neutrophils (light blue arrows), fibroblasts (dark blue arrows), fibrocytes (yellow arrows), and collagen fibers (brown arrows). Scale bars: 200 μm (top), 50 μm (bottom). (E) Masson staining of tissue from different groups on day 12. Scale bars: 200 μm (top), 50 μm (bottom).

burden of more than 9.6×10^6 CFU g^{-1} and 9.2×10^6 CFU g^{-1} on day 1, respectively. 1.9×10^6 CFU g^{-1} of bacterial colonies still present by day 12. However, the Van or ACR-DME+L groups significantly inhibited bacterial growth with 9.7×10^3 CFU g^{-1} and 8.3×10^3 CFU g^{-1} of bacterial colonies remaining by day 12, respectively. Compared to the other four groups, the ACR-DM-HS+L group showed fewer bacterial colonies from day 1 to day 7. Remarkably, bacterial colonies were virtually undetectable by day 12, demonstrating significantly stronger antibacterial properties.

Inflammatory factors in the serum, such as TNF-α and IL-6, were analyzed on day 3 to assess inflammation levels (Figure S28). Compared with the control group, ACR-DM-HS barely reduced TNF-α and IL-6 levels due to the ongoing MRSA infection and inflammation. Although Van killed the bacteria, it can hardly inhibit inflammatory factors soon, and the inflammation was still persistence. In contrast, although ACR-DME+L efficiently killed MRSA, TNF-α and IL-6 levels increased due to excessive ROS generated by ACR-DME-mediated PDT. In comparison,

10.1002/anie.202507833

RESEARCH ARTICLE

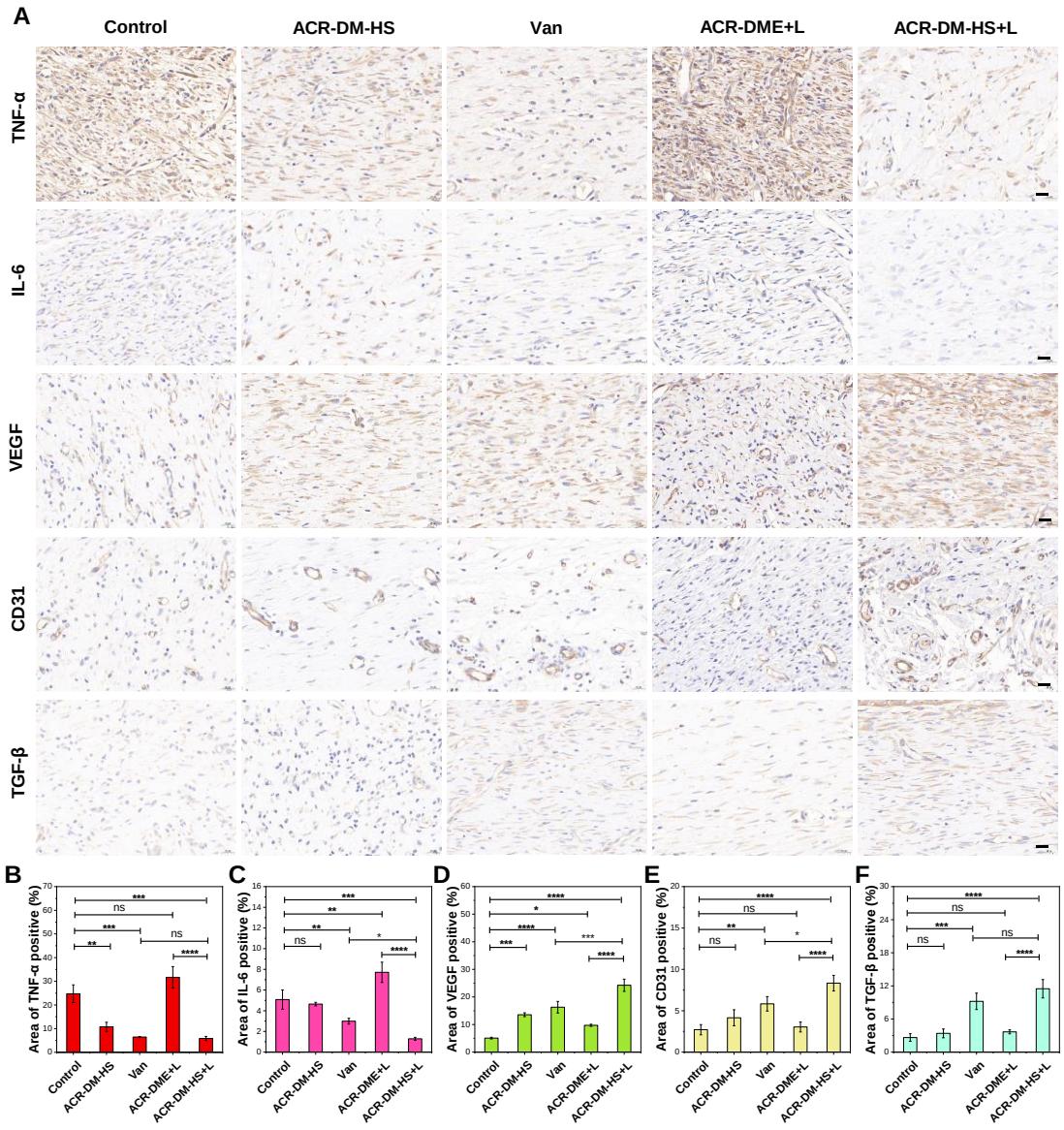

Figure 9. The anti-inflammatory and angiogenesis performance of different treatment. (A) Immunohistochemical staining of TNF-α, IL-6, VEGF, CD31 and TGF-β in infected tissues after 12 days of treatment Scale bars: 20 μm. Quantitative analysis of the levels of TNF-α (B), IL-6 (C), VEGF (D), CD31 (E) and TGF-β (F) from Figure 9A. The data were presented as the means ± SDs (n = 3) and were analyzed by one-way ANOVA with GraphPad Prism software. ns means no significance; *p < 0.05; **p < 0.01; ***p < 0.001; ****p < 0.0001.

ACR-DM-HS-mediated synergistic therapy greatly reduced TNF-α and IL-6 levels. Furthermore, H_2S release was confirmed in ACR-DM-HS-treated wound tissues (Figure S29). These results indicated that following its antibacterial effect through VDA and PDT, ACR-DM-HS efficiently reduced oxidative stress caused by ROS and lowered the expression of pro-inflammatory factors through H_2S release, thereby mitigating the inflammatory side effects.

Haematoxylin and eosin (H&E) and Masson staining were carried out to evaluate the pathological changes in the wound tissues on day 12. As shown in Figure 8D, both the control group and the ACR-DM-HS group lacked an epidermal layer and exhibited extensive inflammatory responses characterized by obvious infiltration of inflammatory cells. In contrast, the Van and ACR-DME+L groups showed a restored epidermal layer with reduced inflammatory cell presence, indicating that inflammation was alleviated through the elimination of pathogenic bacteria. Notably, the ACR-DM-HS+L group not only eliminated all inflammatory cells but also exhibited visible accessory structures, such as hair follicles, sebaceous glands with a greater abundance of collagen fibers, suggesting excellent antibacterial, anti-inflammatory, and wound-healing properties (Figure 8E and Figure S30).

On day 12, immunohistochemical analysis of infected tissue was conducted to assess inflammation, angiogenesis and wound healing (Figure 9A). TNF-α and IL-6 were evaluated to determine inflammation levels in the wounds. The ACR-DM-HS group showed a partial reduction in TNF-α compared to the control

group, while IL-6 levels remained similar to those in the control group, which may be due to the persistent MRSA infection. Due to Van's sustained antibacterial effect, both inflammatory factors were significantly reduced. In contrast, both inflammatory cytokines were significantly elevated in the ACR-DME+L group, while their expression was markedly suppressed in the ACR-DM-HS+L group. Although ACR-DME+L effectively eliminated local pathogens, the PDT process exacerbated inflammation due to excessive ROS. In contrast, ACR-DM-HS+L not only significantly eliminated MRSA through VDA and PDT but also alleviated the side effects of ROS by releasing H_2S (Figure 9B-9C).

Vascular endothelial-derived growth factor (VEGF) is a potent proangiogenic factor that plays a multifunctional role in tissue repair through angiogenesis, epithelial regeneration, and extracellular matrix remodeling.[44] Platelet endothelial cell adhesion molecule-1 (CD31) is a marker for neovascularization.[45] Transforming growth factor-β (TGF-β) can activate fibroblasts to promote collagen accumulation and wound healing.[46] As depicted in Figure 9D-9F, the highest levels of VEGF, CD31 and TGF-β expression were observed in the ACR-DM-HS+L group. These effects were attributed to ACR-DM-HS's ability to enhance angiogenesis via H_2S release after antibacterial treatment, thereby accelerating the healing of diabetic wounds.

The biocompatibility of the treatments was also evaluated. All mice with different treatment showed a gradual increase in weight (Figure S31). Furthermore, as shown in Figure S32 and S33, no significant pathological changes were detected in liver function indices (alanine transferase (ALT), aspartate transferase (AST)), kidney function indices (creatinine (CREA), urea (UREA)), or the histological structures of major organs (heart, liver, spleen, lungs, and kidneys. These results collectively demonstrate that ACR-DM-HS has good biocompatibility.

Conclusion

In summary, a multifunctional MM, ACR-DM-HS, was successfully designed and developed for synergistic therapy of multidrug-resistant bacteria-infected chronic wounds. This innovative system integrates a lipophilic cationic MM with an H_2S donor, combining dual therapeutic modalities. The lipophilic cationic moiety enables targeted bacterial membrane binding via synergistic hydrophobic and electrostatic interactions. Notably, the flexible molecular rotor and extended π-conjugated system endow ACR-DM-HS with unique vibrational properties, enabling light-triggered whole-molecule vibrations that disrupt membrane integrity through VDA. Unlike conventional antibiotics, ACR-DM-HS simultaneously generates VDA and PDT under illumination, effectively bypassing bacterial resistance mechanisms. The strategically incorporated H_2S donor modulates molecular polarity, enhancing membrane binding through two distinct mechanisms: (1) reducing electrostatic interaction energy during initial contact and (2) optimizing van der Waals forces at equilibrium. This dual-phase binding enhancement significantly improves antibacterial efficacy against both G+ and G-. Following microbial eradication, ACR-DM-HS releases H_2S via mitochondrial enzyme-activated processes in infected tissues, ensuring precise therapeutic delivery while preserving antibacterial potency. H_2S can prominently eliminate excess ROS in cell, reduce oxidative stress, lower inflammation levels, and promote cell proliferation and angiogenesis. *In vivo* MRSA-infected diabetic ulcer, ACR-DM-HS highly effectively obliterated MRSA, lowered the inflammatory factor, elevated proangiogenic factor and neovascularization, activated fibroblasts to promote collagen accumulation and wound healing. This synergistic and smart therapy strategy through disruption membrane, generation ROS and releasing H_2S is fascinating for spatiotemporally controllable antibacterial, anti-inflammatory, promoting revascularization and accelerating wound healing. The integrated light-driven mechanical action and PDT not only enhance antibacterial efficacy against multidrug-resistant strains but also minimize resistance development. This work provides a blueprint for designing intelligent antibacterial materials to combat persistent infections and establishes a promising therapeutic paradigm for chronic wound management.

Supporting Information

All data are available in the main text or the Supporting Information.

Acknowledgements

This work was financially supported by the National Natural Science Foundation of China (22177094 and 22174117), and the Fundamental Research Funds for the Central Universities (YJ202419).

Conflict of interest

The authors M.-Y.W., Y.C., and X.-Q.Y. declare that they have filed a Chinese patent application (2024108606672) based on the findings in this paper. Other authors declare no conflict of interest.

Keywords: Chronic wound • light-active molecular machine • photodynamic therapy • hydrogen sulfide

[1] a) V. Falanga, R. R. Isseroff, A. M. Soulika, M. Romanelli, D. Margolis, S. Kapp, M. Granick, K. Harding, *Nat. Rev. Dis. Primers* **2022**, *8*, 50; b) R. M. Mizelle, The *Lancet* **2021**, *397*, 1256; c) C. Wang, E. Shirzaei Sani, C. D. Shih, C. T. Lim, J. Wang, D. G. Armstrong, W. Gao, *Nat. Rev. Mater.* **2024**, *9*, 550.

[2] a) A. Uberoi, A. McCready-Vangi, E. A. Grice, *Nat. Rev. Microbiol.* **2024**, *22*, 507; b) F. Zhao, Y. Su, J. Wang, S. Romanova, D. J. DiMaio, J. Xie, S. Zhao, *Adv. Mater.* **2023**, *35*, 2208069; c) K. Bae, W. Zheng, Y. Ma, Z. Huang, *Theranostics* **2019**, *9*, 1348.

[3] a) D. G. Armstrong, T.-W. Tan, A. J. M. Boulton, S. A. Bus, *JAMA* **2023**, *330*, 62; b) M. Xue, R. Zhao, H. Lin and C. Jackson, *Adv. Drug Deliv. Rev.* **2018**, *129*, 219.

[4] a) P. Ma, C. Y. Yang, C. Li, P. Hu, F. Yang, J. Lu, Y.-Y. Huang, H. Wu, Q. Wu, Y. Pan, X. Wang, *Adv. Fiber Mater.* **2024**, *6*, 543; b) Z. Hu, J. Shan, Y. Cui, L. Cheng, X. L. Chen, X. Wang, *Adv. Healthcare Mater.* **2024**, *13*, 2400101; c) B. Guo, R. Dong, Y. Liang, M. Li, *Nat. Rev. Chem.* **2021**, *5*, 773.

[5] X.-L. Lei, K. Cheng, Y. Li, Z.-T. Zhong, X.-L. Hou, L.-B. Song, F. Zhang, J.-H. Wang, Y.-D. Zhao, Q.-R. Xu, *Chem. Eng. J.* **2023**, *462*, 142222.

[6] H. Peng, D. Rossetto, S.S. Mansy, M.C. Jordan, K.P. Roos, I. A. Chen, *ACS Nano* **2022**, *16*, 4756.

[7] a) C. Elian, R. Méallet, D. L. Versace, *Adv. Funct. Mater.* **2024**, *34*, 2407228; b) Y.-Y. Wang, J.-M. Xiong, L.-W. Xin, Y.-Y. Li, H. Huang, W.-J. Miao, *Chinese Chem. Lett.* **2025**, *36*, 110003.

[8] J. Xi, G. Wei, L. An, Z. Xu, Z. Xu, L. Fan, L. Gao, *Nano Lett.* **2019**, *19*, 7645.

[9] X. Luo, L. Zhang, Y. Luo, Z. Cai, H. Zeng, T. Wang, Z. Liu, Y. Chen, X. Sheng, A. E. D. G. Mandlate, Z. Zhou, F. Chen, L. Zheng, *Adv. Funct. Mater.* **2023***, 26,* 2214036.

[10] L. Huelsboemer, L. Knoedler, A. Kochen, C. T. Yu, H. Hosseini, K. S. Hollmann, A. E. Choi, V. A. Stögner, S. Knoedler, H. C. Hsia, B. Pomahac, M. Kauke-Navarro, *Mil. Med. Res.* **2024**, *11*, 23.

[11] a) M. Kharaziha, A. Baidya, N. Annabi, *Adv. Mater.* **2021**, *33*, 2100176; b) X. Zhou, P. Zhang, H. Ding, H. Wang, Z. Gu, *Nano Today* **2024**, *56*, 102225; c) A. Panáček, L. Kvítek, M. Smékalová, R. Večeřová, M. Kolář, M. Röderová, F. Dyčka, M. Šebela, R. Prucek, O. Tomanec, R. Zbořil, *Nat. Nanotechnol.* **2018**, *13*, 65.

[12] a) X. Zhao, D. Pei, Y. Yang, K. Xu, J. Yu, Y. Zhang, Q. Zhang, G. He, Y. Zhang, A. Li, Y. Cheng, X. Chen, *Adv. Funct. Mater.* **2021**, *31*, 2009442; b) J. Yang, W. Zeng, P. Xu, X. Fu, X. Yu, L. Chen, F. Leng, C. Yu, Z. Yang, *Acta Biomater.* **2022**, *140*, 206.

[13] a) C. Ayala-Orozco, G. Li, B. Li, V. Vardanyan, A. B. Kolomeisky, J. M. Tour, *Adv. Mater.* **2024**, *36*, 2309910; b) C. Ayala-Orozco, D. Galvez-Aranda, A. Corona, J. M. Seminario, R. Rangel, J. N. Myers, J. M. Tour, *Nat. Chem.* **2024**, *16*, 456; c) M. Guentner, M. Schildhauer, S. Thumser, P. Mayer, D. Stephenson, P. J. Mayer, H. Dube, *Nat. Commun.* **2015**, *6*, 8406.

[14] a) A. L. Santos, D. Liu, A. K. Reed, A. M. Wyderka, A. van Venrooy, J. T. Li, V. D. Li, M. Misiura, O. Samoylova, J. L. Beckham, C. Ayala-Orozco, A. B. Kolomeisky, L. B. Alemany, A. Oliver, G. P. Tegos, J. M. Tour, *Sci. Adv.* **2022**, *8*, eabm2055. b) V. García-López, F. Chen, L. G. Nilewski, G. Duret, A. Aliyan, A. B. Kolomeisky, J. T. Robinson, G. Wang, R. Pal, J. M. Tour, *Nature* **2017**, *548*, 567.

[15] a) Y. Sun, X. Sun, X. Li, W. Li, C. Li, Y. Zhou, L. Wang, B. Dong, *Biomaterials* **2021**, *268*, 120614; b) R. Xu, Y. Fan, J. Gu, W. Cao, R. Deng, Z. Rana, X. Lu, C. Xu, G. Xiang, H. Li, X. Wang, *Adv. Funct. Mater.* **2024**, *34*, 2401307.

[16] a) X. Fang, J. Wang, C. Ye, J. Lin, J. Ran, Z. Jia, J. Gong, Y. Zhang, J. Xiang, X. Lu, C. Xie, J. Liu, *Nat. Commun.* **2024**, *15*, 9071; b) H. Ding, J. Chang, F. He, S. Gai, P. Yang, *Adv. Healthcare Mater.* **2022**, *11*, 2101984; c) M. He, Z. Wang, D. Xiang, D. Sun, Y. K. Chan, H. Ren, Z. Lin, G. Yin, Y. Deng, W. Yang, *Adv. Mater.* **2024**, *36*, 2405659.

[17] a) Y. Chen, R. Zhao, C. Tang, C. Zhang, W. Xu, L. Wu, Y. Wang, D. Ye, Y. Liang, *Angew. Chem. Int. Ed.* **2022**, *61*, e202112734; b) P. Shan, J. Liao, J. Li, C. Wang, J. Zhou, L. Mei, Y. Dai, Q. Wang, W. Yin, *Chinese Chem. Lett.* **2024**, *35*, 108545.

[18] a) J. Tian, B. Huang, L. Xia, Y. Zhu, W. Zhang, *Adv. Sci.* **2024**, *11*, 2305183; b) J. Chen, Z. Mu, D. Chen, C. Huang, T. Jin, L. Li, Y. Zeng, Q. Zhou, Y. Zhang, H. Mao, H. Deng, X. Shen, H. Yang, X. Cai, *Chem. Eng. J.* **2023**, *469*, 143985.

[19] a) Y. Huang, Y. Huang, Z. Wang, S. Yu, H. M. Johnson, Y. Yang, M. Li, J. Li, Y. Deng, K. Liang, *Small* **2023**, *19*, 2304324; b) M. He, Z. Wang, D. Xiang, D. Sun, Y. K. Chan, H. Ren, Z. Lin, G. Yin, Y. Deng, W. Yang, *Adv. Mater.* **2024**, *36*, 2405659; c) A. Domán, É. Dóka, D. Garai, V. Bogdándi, G. Balla, J. Balla, P. Nagy, *Redox Biol.* **2023**, *60*, 102617.

[20] a) E. Glukhov, M. Stark, L. L. Burrows, C. M. Deber, *J. Biol. Chem.* **2005**, *280*, 33960; b) M. P. Hughes, *Integ. Biol.* **2024**, *16*, zyae003. c) J. Li, J. Li, J. He, X. He, D. Chen, Z. Dong, L. Xiong, W. Bai, M. Li, R. Guo, Q. He, *Nano Res.* **2024**, *17*, 9932; d) Y. Zhang, M. Luo, X. Shi, A. Li, W. Zhou, Y. Yin, H. Wang, W.-L. Wong, X. Feng, Q. He, *Sci. Adv.* **2024**, *10*, eadp4872; e) H. Bai, H. Yuan, C. Nie, B. Wang, F. Lv, L. Liu, S. Wang, *Angew. Chem. Int. Ed.* **2015**, *54*, 13208.

[21] a) J. L. Wang, X. Pan, X. Li, K. M. Liu, M. Yao, J. Y. An, Y. Wan, X. Q. Yu, S. Feng, M.-Y. Wu, *Adv. Mater.* **2024**, *6*, 2411468; b) L. Chen, M.-Y. Wu, S.-L. Chen, R. Hu, Y. Wang, W. Zeng, S. Feng, M. Ke, L. Wang, S. Chen, M. Gu, *Adv. Mater.* **2024**, *36*, 2407268; c) J. L. Wang, F.-W. Xia, Y. Wang, H. Z. Shi, L. J. Wang, Y. Zhao, J. X. Song, M.-Y. Wu, S. Feng, *ACS Appl. Mater. Interfaces* **2023**, *15*, 17433; d) M.-Y. Wu, A. Y. H. Wong, J.-K. Leung, C. Kam, K. L.-K. Wu, Y.-S. Chan, K. Liu, N. Y. Ip, S. Chen, *Proc. Natl. Acad. Sci. U.S.A.* **2021**, *118*, e2106143118; e) M.-Y. Wu, Z.-J. Wu, J.-L. Wang, C. Kam, T. Y. Chou, S. Feng, K. Li, S. Chen, *ACS Mater. Lett.* **2024**, *6*, 4533; f) M.-Y. Wu, J.-K. Leung, L. Liu, C. Kam, K. Y. K. Chan, R. A. Li, S. Feng, S. Chen, *Angew. Chem. Int. Ed.* **2020**, *59*, 10327.

[22] F. W. Xia, B. W. Guo, Y. Zhao, J. L. Wang, Y. Chen, X. Pan, X. Li, J. X. Song, Y. Wan, S. Feng, M.-Y. Wu, *Adv. Mater.* **2023**, *35*, 2309797.

[23] a) A. Lauchner, A. E. Schlather, A. Manjavacas, Y. Cui, M. J. McClain, G. J. Stec, F. J. García de Abajo, P. Nordlander, N. J. Halas, *Nano Lett.* **2015**, *15*, 620; b) Y. Cui, A. Lauchner, A. Manjavacas, F. J. García de Abajo, N. J. Halas, P. Nordlander, *Nano Lett.* **2016**, *16*, 6390.

[24] a) T. Shigematsu, K. Koshiyama, S. Wada, *Sci. Rep.* **2015**, *5*, 15369; b) F. Li, C. U. Chan, C. D. Ohl, *Biophys. J.* **2013**, *105*, 872.

[25] a) B. Li, D. Wang, M. M. S. Lee, W. Wang, Q. Tan, Z. Zhao, B. Z. Tang, X. Huang, *ACS Nano* **2021**, *15*, 1385.

[26] a) S. K. Chung, J. Jung, *Photochem. Photobiol.* **1995**, *61*, 383; b) B. B. Fischer, A. Krieger-Liszkay, R. I. L. Eggen, Environ. *Sci. Technol.* **2004**, *38*, 630; c) Z. Liu, Q. Wang, W. Qiu, Y. Lyu, Z. Zhu, X. Zhao, W. H. Zhu, *Chem. Sci.* **2022**, *13*, 3599.

[27] J. Liang, X. Ran, Y. Liu, X. Yu, S. Chen, K. Li, *J. Mater. Chem. B* **2024**, *12*, 3686.

10.1002/anie.202507833

[28] X. Shi, S. H. P. Sung, J. H. C. Chau, Y. Li, Z. Liu, R. T. K. Kwok, J. Liu, P. Xiao, J. Zhang, B. Liu, J. W. Y. Lam, B. Z. Tang, *Small Methods* **2020**, *4*, 2000046.

[29] a) M.-Y. Wu, L. J. Wang, C.-M. Qin, Y. Wang, J. X. Song, Y. Zhao, Y. Wan, S. Feng, *Sens. Actuators B Chem.* **2023**, *381*, 133471; b) Z. Gao, X. Zheng, W. Liu, J. Sha, S. Bian, H. Ren, J. Wu, W. Zhang, C.-S. Lee, P. Wang, *Chinese Chem. Lett.* **2025**, *36*, 109874.

[30] J. Zhuang, Z. Ma, N. Li, H. Chen, L. Yang, Y. Lu, K. Guo, N. Zhao, B. Z. Tang, *Adv. Mater.* **2024**, *36*, 2309488.

[31] X. Gong, Y. Han, T. Wang, G. Song, H. Chen, H. Tang, X. Huang, K. Deng, S. Wang, Y. Wang, *Adv. Mater.* **2024**, *37*, 2414357.

[32] X. Zhou, P. Zhang, H. Ding, H. Wang, Z. Gu, *Nano Today*, **2024**, *56*, 102225.

[33] J. L. Wang, Y. Chen, J. X. Song, B.-W. Guo, F.-W. Xia, Y. Wan, W. X. Wu, C. Zhang, S. Feng, M.-Y. Wu, *Adv. Funct. Mater.* **2024**, *34*, 2312162.

[34] H. Y. Heo, G. Zou, S. Baek, J. S. Kim, E. Mylonakis, F. M. Ausubel, H. Gao, W. Kim, *Adv. Sci.* **2024**, *11*, 2306112.

[35] a) J. Yang, Z. Zhai, J. Liu, C. Weng, *J. Appl. Polym. Sci.* **2021**, *138*, 50105; b) A. U. Mahmood, Y. G. Yingling, *J. Chem. Theory Comput.* **2022**, *18*, 3122.

[36] M. Wu, C. Chen, Z. Liu, J. Tian, W. Zhang, *Acta Biomater.* **2022**, *142*, 242.

[37] M. Yang, Z. Özdemir, H. Kim, S. Nah, E. Andris, X. Li, Z. Wimmer, J. Yoon, *Adv. Healthcare Mater.* **2022**, *11*, 2200529.

[38] a) J. Jia, Z. Wang, M. Zhang, C. Huang, Y. Song, F. Xu, J. Zhang, J. Li, M. He, Y. Li, G. Ao, C. Hong, Y. Cao, Y. E. Chin, Z.-c. Hua, J. Cheng, *Sci. Adv.* **2025**, *6*, eaaz5752; b) M. Lee, V. Tazzari, D. Giustarini, R. Rossi, A. Sparatore, P. Del Soldato, E. McGeer, P. L. McGeer, *J. Biol. Chem.* **2010**, *285*, 17318-1732; c) J. Cheng, Y. Zhu, Y. Dai, L. Li, M. Zhang, D. Jin, M. Liu, J. Yu, W. Yu, D. Su, *Angew. Chem. Int. Ed.* **2023**, *62*, e202304312; d) X. Zheng, H. Li, S. Gao, K. Müllen, J. Zhang, C. Ji, M. Yin, *Small* **2024**, 2403284; e) K. Cheng, B. Liu, X. S. Zhang, R. Y. Zhang, F. Zhang, G. Ashraf, G. Q. Fan, M. Y. Tian, X. Sun, J. Yuan, *Nat. Commun.* **2022**, *13*, 4567.

[39] Q. Ou, X. Qiao, Z. Li, L. Niu, F. Lei, R. Cheng, T. Xie, N. Yang, Y. Liu, L. Fu, J. Yang, X. Mao, X. Kou, C. Chen, S. Shi, *Cell Metab.* **2024**, *36*, 78.

[40] a) L. B. Case, M. A. Baird, G. Shtengel, S. L. Campbell, H. F. Hess, M. W. Davidson, C. M. Waterman, *Nat. Cell Biol.* **2015**, *17*, 880; b) T. Wei, T. Pan, X. Peng, M. Zhang, R. Guo, Y. Guo, X. Mei, Y. Zhang, J. Qi, F. Dong, M. Han, F. Kong, L. Zou, D. Li, D. Zhi, W. Wu, D. Kong, S. Zhang, C. Zhang, *Nat. Nanotechnol.* **2024**, *19*, 1178; c) Y. Kang, L. Xu, J. Dong, X. Yuan, J. Ye, Y. Fan, B. Liu, J. Xie, X. Ji, *Nat. commun.* **2024**, *15*, 1042.

[41] Y. Gao, Y. Deng, W. Geng, S. Xiao, T. Wang, X. Xu, M. Adeli, L. Cheng, L. Qiu, C. Cheng, *Adv. Mater.* **2024**, *36*, 2408787.

[42] Y. Cai, K. Chen, C. Liu, X. Qu, *Bioact. Mater.* **2023**, *28*, 243.

[43] C. Oh, W. Lee, J. Park, J. Choi, S. Lee, S. Li, H. N. Jung, J. S. Lee, J. E. Hwang, J. Park, *ACS nano* **2023**, *17*, 4327.

[44] R. S. Apte, D. S. Chen and N. Ferrara, *Cell* **2019**, *176*, 1248.

[45] a) M.-Y. Wu, X. Xu, R. Hu, Q. Chen, L. Chen, Y. Yuan, J. Li, L. Zhou, S. Feng, L. Wang, *Adv. Sci.* **2023**, *10*, 2207736; b) J. Wang, X. Ge, Y. Xiang, X. Qi, Y. Li, H. Xu, E. Cai, C. Zhang, Y. Lan, X. Chen, Y. Shi, Z. Li, J. Shen, *Chinese Chem. Lett.* **2025**, *36*, 109819.

[46] J. Massagué, D. Sheppard, *Cell* **2023**, *186*, 4007.

10.1002/anie.202507833

Entry for the Table of Contents

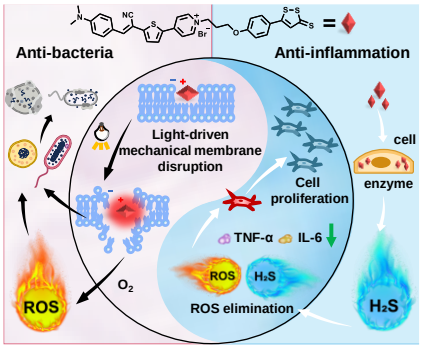

A novel H_2S donor functionalized molecular machine, ACR-DM-HS, with combination of antibacteria and anti-inflammation to accelerate angiogenesis through membrane disruption, ROS generation and H_2S releasing was developed for synergistic therapy of multiple resistant bacteria-infected chronic wound, which offers a promising treatment approach for combating bacterial multidrug resistance and tackling chronic wounds.